Supplementary Information (SI) for Materials Horizons.

Supporting Information

Lignin-derived Carbon Dots Upgraded Bacterial Cellulose Membrane as All-in-one Interfacial Evaporator for Solar-driven Water Purification

Nirmiti Mate [a], Kallayi Nabeela [a], Gopika Preethikumar [c,d], Saju Pillai* [c,d] and Shaikh M. Mobin* [ab].

[a] Department of Chemistry, Indian Institute of Technology Indore, Simrol, Khandwa Road, Indore 453552, India.

[b] Centre for Advanced Electronics (CAE), Indian Institute of Technology (IIT) Indore, Simrol, Khandwa Road, Indore 453552, India

[c] Materials Science and Technology Division, CSIR-National Institute for Interdisciplinary Science and Technology (NIIST), Thiruvananthapuram, Kerala 695 019, India.

[d] Academy of Scientific and Innovative Research (AcSIR), Ghaziabad 201002, India

*Corresponding author

Email: xray@iiti.ac.in (Shaikh M. Mobin)

Tel.: +91-731-2438752

1. Experimental Section

1.1 Materials and Reagents:

Lignin was purchased from TCI, sodium chloride (NaCl) ethylenediamine (EDA) and methylene blue (MB), methyl orange (MO), congo red (CR) and rhodamine B (RB) were procured from Sigma-Aldrich. Kombucha and tea powder were purchased from local market. $CoSO_4 \cdot H_2O$, $FeCl_2$, $AgNO_3$, and $CdCl_2$ were purchased from Loba. Dextrose, epichlorohydrin (ECH), sodium hydroxide (NaOH) and tetracycline (TET) and doxycycline (DOX) are obtained from SRL. All the chemical were of analytical grade and used without further purification. Deionized water (DI) was used throughout the experiment.

1.2 **Preparation of Bacterial Cellulose (BC)**

The kombucha strains were acquired online and tea powder were purchased from regional market. Black tea powder was mixed to 1000 mL water and boil for 5 min. After obtaining the tea solution, it was cooled and remove the tea leave via filtration. Then add 60 g dextrose to form the culture media for Kombucha. A piece of kombucha (10 cm diameter) was the added to the above freshly prepared growth medium and kept for culturing for 7 days in static condition maintaining the 30 °C. After completion of BC growth, a brown-colored BC pellicle was harvested from the air liquid interface. Impure BC pellicle was washed first with water and then allowed to was thoroughly with 2 % NaOH to eliminate the attached bacterial cells and other impurities. Following washing, the BC membranes were stored in water at -4 °C prior to use.

1.3 Synthesis of N-LCDs

A N-doped lignin derived Carbon dots (N-LCDs) were synthesized from 0.6 g lignin powder which were dissolved in 25 mL of DI water and added 5 mL of EDA as a doping agent. Treat the above reaction mixture at 180 °C for 12 h hydrothermally. The obtained solution in reaction mixture were centrifuged with 10000 rpm for 30 min to remove the settled debris and then dialysed against the DI water for 24 h. The purified CDs solution thus obtained was used for further studies.

1.4 In-situ synthesis of BC@N-LCDs (without cross-linking)

The 2.4 g of lignin powder was dissolved in 70 mL of DI water and 20 mL of EDA was further added to this solution. After ensuring complete dissolution of both reagents, as the above-obtained BC pellicle (~5.1 cm diameter, ~0.8 cm thickness) was added and treated them hydrothermally at 180 °C for 12 h. After the reaction, BC@N-LCD was wash out against distilled water under continuous stirring for 24 h.

1.5 Cross-linking of BC@N-LCDs with ECH

To overcome the problem of leaching the BC@N-LCD were cross-linked with ECH. For the same take 2.4 g lignin dissolved in 70 mL of DI, add BC (5.1 cm diameter 0.8 cm thickness) followed by stirring at 1000 RPM for 30 mins while heating gently. This is to ensure complete imbibition of lignin solution. To this mixture add 6 mL of 12 wt% NaOH and 1.2 mL of ECH. Then transfer the obtained solution in teflon-lined stainless steel hydrothermally and add 20 mL of EDA into it as doping agent and treated them hydrothermally for 12 h at 180 °C. The obtained black colored *c*-BC@N-LCD hydrogel was washed with distilled water several times under continuous stirring.

1.6 Characterization Technique:

The morphological analysis of *c*-BC@N-LCD was carried out using scanning electron microscope (SEM), Carl Zeiss, Germany, with an accelerating voltage of 10 kV. Aerogel samples (obtained after lyophilization of hydrogels) for SEM were prepared by cutting using a sharp razor and stuck on a carbon tape. Samples were gold-sputtered prior to the imaging to avoid charging. Long BC fibres and the distribution of aggregate N-LCD in the BC matrix were visualized on an FEI Tecnai 30 G2S-TWIN transmission electron microscope (TEM) operated at an accelerating voltage of 300 kV. TEM sample preparations were done on a carbon-coated copper grid by drop-casting two to three drops of the well dispersed dilute sample solution. The crystallinity of BC was determined from the wide-angle X-ray scattering (WAXS) measurements carried out on a Xeuss SAXS/WAXS system using a Genisxmicro source from Xenocs operated at 50 kV and 0.6 mA. The powder X-ray diffraction (XRD) pattern of the N-LCD sample was taken on a PANalytical Empyrean instrument equipped with reference radiation of Cu Kα (λ = 1.54 Å) at an operating voltage of 45 kV. Xray photoelectron spectroscopy (XPS) was done to know about the chemical functionality and composition of N-LCDs, BC, BC@N-LCD and *c*-BC@N-LCD using PHI 5000 VersaProbe II, ULVAC-PHI Inc., USA) equipped with micro-focused (100 μm, 15 kV) monochromatic Al-Kα X-Ray source (hν = 1486.6 eV). XPS spectra were processed using PHI's Multipak software. The binding energy was referenced to the C 1s peak at 284.8 eV. The attenuated total reflectance-Fourier transform infrared (ATR-FTIR) spectra were recorded with a Bruker Alpha II system over the wavenumber range of 4000−500 cm^{-1}. Absorption, total reflectance, and diffuse reflectance spectra (DRS) of N-LCD and BC@N-LCD and *c*-BC@N-LCD were recorded in the 200−2500 nm range, using a UV−VIS−NIR spectrometer (UV-2600). The measurements were corrected by the baseline/blank correction. The NIR solar reflectance (R*) was measured using the solar spectral irradiance in the range 700−2000 nm. The solar absorptions "A" of samples in the 700−2000 nm region were measured using eq 1.

$$A = \frac{\int (1 - T).S.d\lambda}{\int S.d\lambda} \qquad (1)$$

Where T is the reflectance of the sample, S is the solar spectral irradiance (Wm^{-2} nm^{-1}), and λ is the wavelength. The wettability of samples was checked using a contact angle goniometer (KYOWA, DMe-201) by sessile-dropping water (2.0 μL) droplets on the porous BC@N-LCD. The specific surface areas of the aerogels were measured by the Brunauer−Emmett−Teller

(BET) method using Autosorb-1C (AX1C-MP-LP) at 298 K. The pore size distribution was obtained by the Barrett−Joyner−Halenda (BJH) method. DSC measurements for finding latent heat of vaporization were acquired on a PerkinElmer DSC 8000 instrument using aluminum hermetic sample pan at a scan rate of 5°C/min. Concentration of metal ions in the purified water sample were found out by (Inductively coupled plasma mass spectrometry) ICP-MS analysis performed in Thermo Scientific iCAP RQ spectrometer.

1.7 Estimation of Photothermal Energy Conversion

The evaporation experiments were performed at room temperature under a xenon lamp (250 W) solar simulator coupled with a Newport monochromator (Newport Instruments). For water evaporation studies, *c*-BC@N-LCD and the control BC with ∼0.8 cm thickness and ∼5.1 cm diameter was used. *c*-BC@N-LCD were kept on a pure BC pellicle and allowed to append on normal tap water in a petri dish. The size of the petri dish was selected to fit the fabricated *c*-BC@N-LCD inside it. The approximate power density at the evaporating surface was kept as 1 kW m^{-2}. The mass loss corresponding to the evaporated water was calculated using an electronic weighing balance (iScale i-400c, India). The temperature profiles before and after illumination were captured on an IR thermal imaging camera (FLIR TG 267). The photothermal energy conversion from solar light into heat for vapor generation was calculated from amount of evaporated water with and without *c*-BC@N-LCD and control BC. Eq. 2 was used to calculate the power necessary for the evaporation of water (Q_e).

$$Q_e = \frac{m \times h_{LV}}{t} (\%) \qquad (2)$$

Where, m is the mass of evaporated water per unit area, t is the time, and h_{LV} is the enthalpy of vaporization of water foe particular evaporating system. h_{LV} of water when evaporating by a hydrogel system was obtained directly from a DSC thermogram of the corresponding hydrogel sample at a heating rate of 5 °C min^{-1} under a nitrogen flow. The h_{LV} of free water was also calculated for comparison from the thermogram of pure water. If Q_s is the power of incident solar radiation monitored in a solar power meter (Newport Instruments, 91159A), the solar evaporation efficiency (η) is obtained as the ratio of Q_e and Q_s (Eq 3)

$$\eta = Q_e/Q_s \qquad (3)$$

The final equation for η in percentage given in Eq 4.

$$\eta = \frac{m \times h_{LV}}{I \times t} \qquad (4)$$

where Q_s = I which is the incident solar power density.

1.8 Real-Time Solar Evaporation Experiments

Practicality of the solar evaporator was tested by performing evaporation experiments outdoor in real-time with a lab made setup on sunny day the with no clouds. To find out the rate solar intensity was continuously monitored every 10 min on a power meter, and the average value was considered for calculations. The rate of evaporation was examined by taking the water from different sources such as lake water, RO water, tap water, pond water and river water. In order to check the per day performance of the prepared evaporator, generated steam was condensed and collected at the end of the day, while the solar power intensity, temperature and humidity were noted each hour.

1.9 Evaporation Rate at Different Water Sources, Desalination and Removal of Pollutants by *c*-BC@N-LCDs

The rate of evaporation was examined by taking the water from different sources such as lake water, RO water, tap water, pond water and river water. The solar evaporation as mentioned above was performed. For seawater desalination the 3.5 % NaCl were used as a feed solution and irradiate the *c*-BC@N-LCD with 1 kW m-2 sun illumination. The loss in weight is measured by weighing balance (iScale i-400c, India) and used to calculate the evaporation rate and evaporation efficiency. To evaluate the removal of heavy metal ions from water, certain amount of wet *c*-BC@N-LCD were added in 50 mL of aqueous solutions containing 2 ppm of $CoSO_4 \cdot H_2O$, $FeCl_2$, $AgNO_3$, and $CdCl_2$, respectively. Each sample simulated water samples were treated with *c*-BC@N-LCD and water the final water samples were collected, followed by measurement of metal ion concentrations through ICP-MS. Similarly, *c*-BC@N-LCD hydrogels were placed separately in aqueous solutions containing; dyes like MO, MB, RB, and CR, etc. (2 ppm each), and pharmaceutical drugs such as TET and DOX (both 10 ppm). Efficacy in water purification in these cases were checked after irradiating the *c*-BC@N-LCD containing evaporating system by sunlight in real time (illumination intensity of ~1 kW/m^2). The decrement in concentration of dyes and pharmaceutical drugs before and after treatment were monitored with UV-visible spectrophotometer.

2. Characterization of Carbon Dots (N-LCDs)

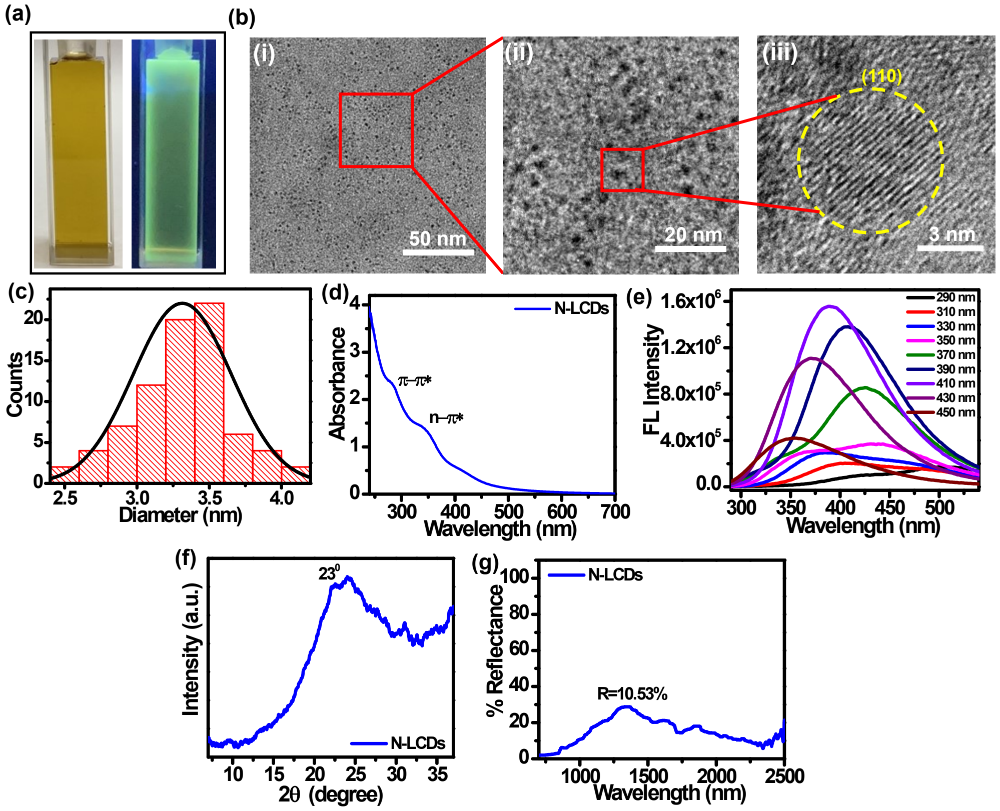

Figure S1. Characterizations of N-LCD: a) digital photographs of N-LCD dispersion captured under bright light (right) and UV light (left), b) TEM images of N-LCD captured at different magnification levels, c) histogram representing size distribution, d) UV-visible absorption spectrum, e) FL spectra taken under varied excitation wavelengths. f) XRD pattern. g) DRS spectrum of N-LCD in NIR range.

3. FTIR and XPS Studies of N-LCDs

The functionalities of N-LCD were examined by FTIR spectrum (Figure S1a). A broad peak from 3350-2851 cm^{-1} is assigned to the combinations of stretching vibrations of O-H/N-H and C-H bonds. Other prominent peaks at 1664 cm^{-1}, 1558 cm^{-1}, 1398 cm^{-1} and 1327 cm^{-1} are assigned to C=O stretching, N-H bending and C-N stretching, aromatic ring vibrations, respectively. The peak at 1185 cm^{-1} is from C-O functionality. Further, the functionalities and chemical composition on N-LCDs was inspected by XPS. XPS survey spectrum of N-LCD (Figure S1b) confirms doping with N elements and chemical composition. The deconvoluted high-resolution (HR) spectra for C1s, O1s, and N1s are provided in Figure S1c-e. In high resolution C1s XPS spectra (Figure S1c), the peak at 284.7, 286.0 and 287.7 eV are attributed to C-C/C=C, C-N/C-O and C=O, respectively. In the high-resolution O1s XPS spectra (Figure S1d) the peaks at 531.5 and 532.8 eV are assigned to C=O and C-O-C/C-OH, respectively. Figure S1e indicate the high resolution spectra of N1s, the peak at 399.5 and 400.8 eV is for pyridinic-N and pyrrolic-N. The surface functionalization of carbon dots (CDs) plays an integral part in their dispersibility in aqueous and organic solvents, as the surface groups of CDs make them either hydrophilic or hydrophobic. Notably, functional groups such as hydroxyl, carboxyl, amines, amide, thiols, etc give CDs hydrophilicity, making them highly dispersible in water. The as-synthesized N-LCDs possess OH/NH, C-H, C=O, C-O groups on their surface, which makes them dispersible in water[1].

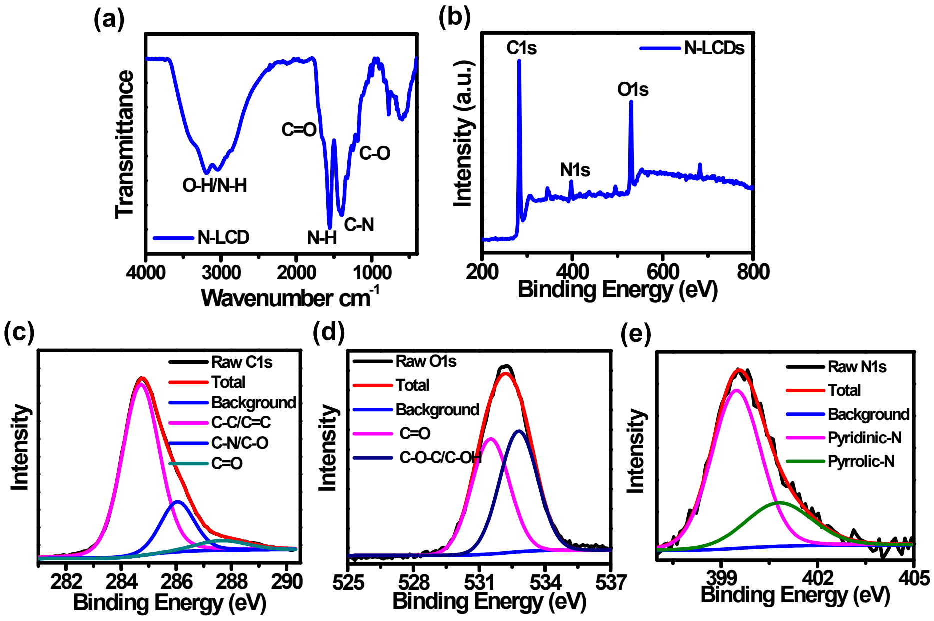

Figure S2. Chemical functional characterization of N-LCDs: a) FTIR, b) XPS survey scan. c-e) Details of XPS deconvoluted spectra of N-LCD

4. Chacaterization of bacterial cellulose (BC):

By culturing the Kombucha strain, BC was produced at the liquid-air interface as a thick pellicle. Figure S2a shows a digital image of a BC pellicle that was procured after multiples steps of purification. Figure S2b represents the robust network structure of a lyophilized BC pellicle as observed in a SEM (a lower magnification image is given in inset). The thicknesses of fibrils are analysed and a histogram is drawn (Figure S2c), showing the width of BC fibril falls in 20-100 nm range. Furthermore, ATR-FTIR spectrum of BC is shown in Figure S2d, featuring all the characteristics peaks of cellulose. The peak at 3352 cm^{-1} arises due to hydroxyl groups (-OH) stretching vibration of BC. The 2895 cm^{-1} is attributed to C-H stretching vibrations. The C–O–C and C–O–H stretching vibrations of pyranose ring are observed at 1035-1059 cm^{-1} [2]. The XPS survey spectrum of BC exhibited two peaks at 284.0 and 530.4 eV, indicative of presence of C and O, respectively (Figure S2e). The HR C1s peak of cellulose (Figure S2f) shows three resolved peaks at 284.7 eV, 286.6 eV and 288.0 eV, assigned to C-

C/C-H sp^3 type carbon, C-O-, and O-C-O, respectively. The HR O1s peak (Figure S2g) confirms the existence of C-O-C (531.2 eV) and C-OH (532.6 eV) functionalities in BC[3].

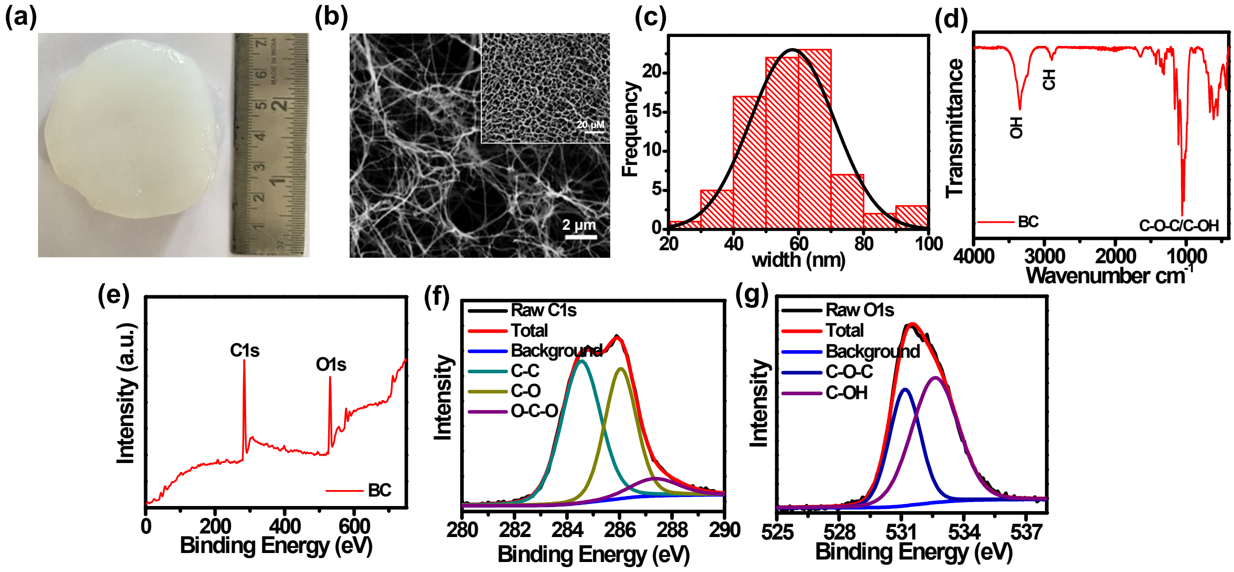

Figure S3. Characterizations of BC: (a) digital photograph, (b) SEM image showing nanofibrous porous network structure, (c) histogram drawn for width of cellulose fibres, (d) ATR-FTIR spectrum, (e) XPS survey scan, (f-g) HR deconvoluted peak for (f) C1s and (g) O1s.

5. Leaching experiment indicating the significance of cross-linking

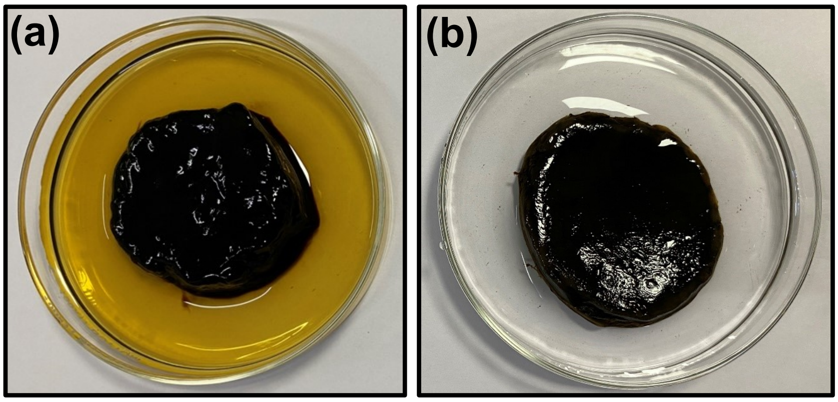

Figure S4. Demonstration of leaching of N-L@CD from the hydrogel composites (a) before (BC@N-LCD) (b) after cross-linking with ECH (*c*-BC@N-LCD).

6. Comparative XPS details of N-LCD, BC@N-LCD and *c*-BC@N-LCD

The XPS survey scan recorded for *c*-BC@N-LCD, non-cross-linked BC@N-LCD, and N-LCD are compared in Figure S5a. All three samples contain peaks corresponds to C1s, N1s and O1s at the peak intensity of 281.6 eV, 398.4 and 531.6 eV, respectively. A comparison of HR C1s peaks of the same samples are also provided in Figure S5b.

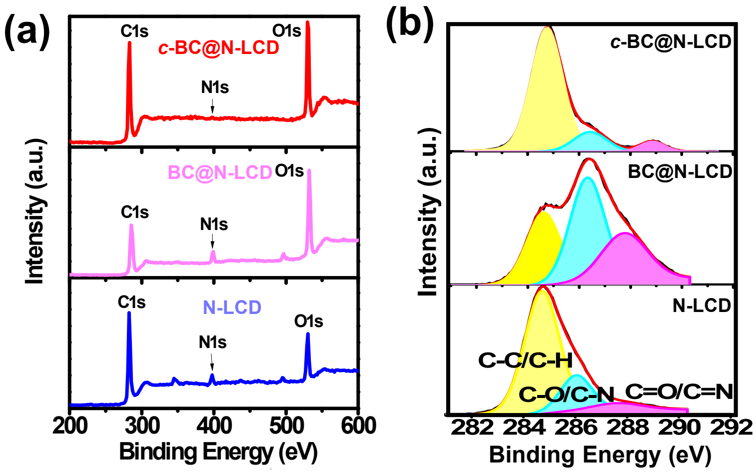

Figure S5. a) XPS survey scan. b) HR scan of C1s.

7. Brunauer, Emmett and Teller (BET) and Barrett-Joyner-Halenda (BJH) analysis

BET surface area plot and BJH pore volume plots of both samples are provided in Figure S6. Though the mesoporosity of photothermal composite was maintained upon incorporation of N-LCD, a reduction in pore volume from 237 Å to 183 Å is evident.

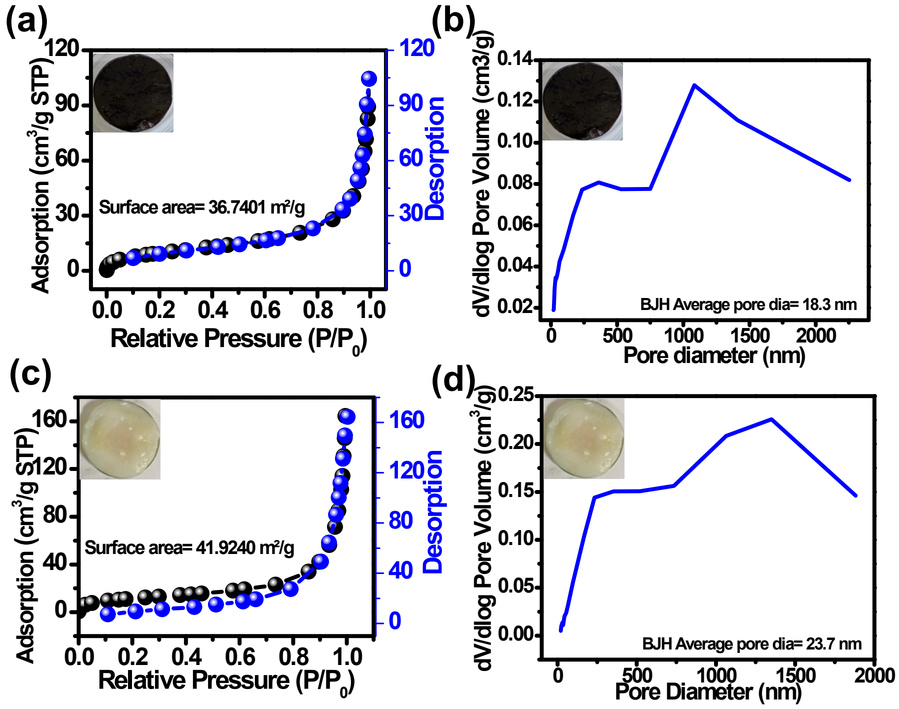

Figure S6. Nitrogen adsorption and desorption analysis conducted for *c*-BC@N-LCD and control pristine BC aerogels: a) BET adsorption isotherms and b) corresponding BJH pore volume plots for *c*-BC@N-LCD. c) BET adsorption isotherms d) corresponding BJH pore volume plots for BC. The digital photographs of the samples analysed are given insets.

8. Contact angle measurements for BC and *c*-BC@N-LCDs

To illustrate the hydrophilic nature of material, wettability studies were carried out as a sessile drop water contact angle experiments on BC (Figure S7a) and *c*-BC@N-LCD (Figure S7b). The good hydrophilic nature of BC and *c*-BC@N-LCD renders quick absorption of water when small drop of water in to contact with hydrogel composite. This support easy wicking of water through the fabricated evaporator. Both mesoporous and microporous nature of the photothermal composite with good hydrophilic nature would therefore be expected to enhance the rate of evaporation by facilitating faster water transport to the points of evaporation.

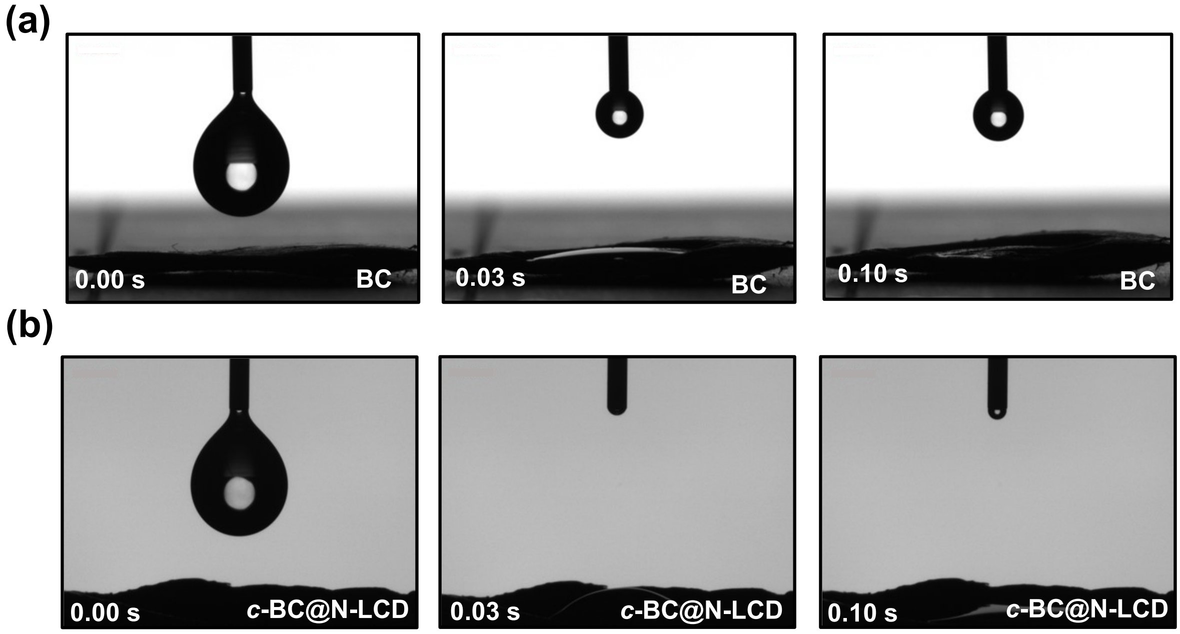

Figure S7. Wettability studies performed by contact angle measurements: (a) BC (b) *c*-BC@N-LCD.

9. **Table S1**. Represents the ER of composite, BC and water.

Sr. No.	**Material**	**Evaporation Rate (kg m^{-2} h^{-1})**
1.	*c*-BC@N-LCD	2.2
2.	BC	0.47
3.	Water	0.40

10. Effect of loading on rate of evaporation

The composition of a photothermal *c*-BC@N-LCD platform consists of 1) N-LCD, responsible for the photothermal activity, 2) cross-linking part connecting each N-LCD and BC, and 3) BC as a matrix. To calculate the active component loading a *c*-BC@N-LCD composite of 2 cm×2 cm×0.4 cm (l×b×h) was taken and compared with the weight of pure BC pellicle of same dimension (mass from crosslinking units were neglected). Thus, % loading with 86%, 80%, 79% and 73% were obtained by varying the amount of lignin precursor as 600 mg, 400 mg, 200 mg and 100 mg, respectively during the preparation of *c*-BC@N-LCD. The loading of 86% was the maximum active component loading possible, above which the cross-linking could not withhold N-LCD to BC matrix. This maximum composition has therefore been selected throughout for the further studies. While checking the evaporation performance on the composition, an obvious increase in the rate of evaporation were observed (Figure S8) because of the more availability of NIR active components on the exposed *c*-BC@N-LCD surface.

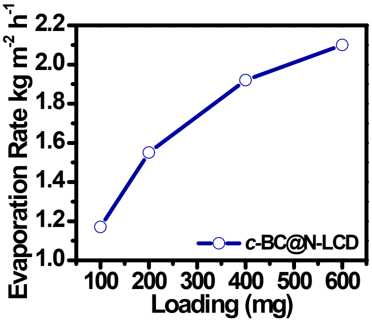

Figure S8. Evaporation rate of *c*-BC@N-LCDs under different loading.

11. Effect of irradiation intensity on evaporation rate

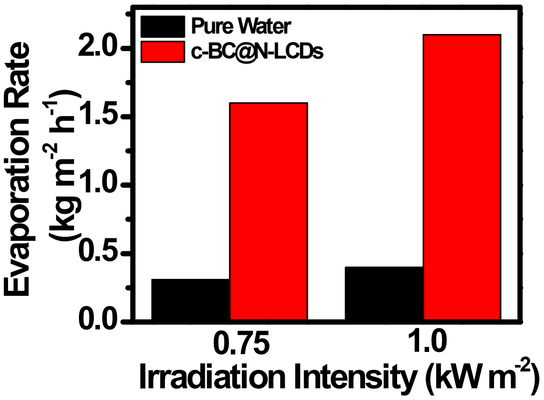

Figure S9. Effect of irradiation intensity on photothermal evaporation performance

12. Table S2. Indicative of different solar evaporator for comparing the composition, Evaporation rate.

Sr. No.	**Sample**	**Composition**	**Evaporation rate (kg m^{-2} h^{-1})**	**Solar irradiation (1 kW m^{-2})**	**Reference**
1.	3D wooden cone evaporator	Tannic acid and iron sulfate hydrate, Poplar veneer	1.79	1	4
2.	Integrated carbon-based aerogel	GO/SWCNTs/SA	1.6	1	5
3.	Biochar-based interfacial systems	Carbonized corn straw	1.4	1	6
4.	Mesoporous interfacial system	Graphite and wood	1.2	1	7
5.	Semiconductor decorated wood membrane	$CuFeSe_2$ N/ wood	1.3	5	8

6.	Water Delivery Channel in solar evaporator	Polyethylene foam and Air-laid paper	1.46	1	9
7.	Hierarchical structures	Suedette sponge, filter paper, and polydopamine	1.8	1	10
8.	Bifunctional MoS_2-based evaporator	MoS_2 nanoflowers, Air-laid paper, Expandable polyethylene	1.27	1	11
9.	Carbon Dot/ Hydrogel	Carboxymethyl cellulose/Chitosan/C-Dots	1.4	1	12
10.	$Au@Bi_2MoO_6$-carbon dots solar steamer	Nanopyramids/ Nanoparticle/Carbon-dots	1.69	1	13
11.	*c*-BC@N-LCDs	Lignin derived CDs and	2.2	1	Present work

		bacterial cellulose			

13. Evaporation efficiency in saline water

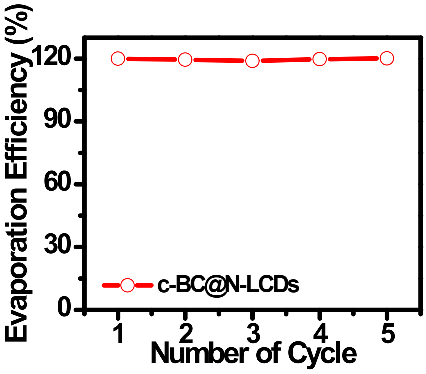

Figure S10. Evaporation efficiency in saline water

14. Removal efficiency of metal ions

Among the various available technique, the adsorption process has evolved as a prominent method for removing pollutants from water system. The removal efficiency of metal ions depends on the phenomenon of adsorption which is affected by many factors such as pH, ionic strength, hard-soft acid base theory and electronegativity, etc. The removal efficiency also depends upon hydrogel morphology and functional groups present on the surface of *c*-BC@N-LCD hydrogel. The hydrogel contains polar functional groups such as hydroxyl, amines and carbonyl, which can bind ions through van der Wal forces, electrostatic interaction, etc. and this could be a most possibly reason behind this removal of metal ions from seed water[14,15].

15. Degradation study of Methylene blue (MB) in presence of *c*-BC@N-LCDs

Primarily, the variation in degradation of different dyes depends on a chemical structure, molecular mass, and surface charge of organic molecules, etc. The molecular weight of dyes is in the order of CR>RhB>MO>MB. So, the rate of degradation for MO, RhB and CR was low because of their high molecular mass as compare to MB. Also, MB is positively charged showing the great electrostatic affinity towards the N-LCDs as compared to other dyes. Secondly, the pH also is one of the factors that influences the degradation of dyes. Due to many surfaces' negative molecules on the surface of N-LCDs it bears negative charge. The methylene blue which is cationic dye degrade easily among all other dyes such as MO because of its anionic nature[14]. Moreover, the efficiency of photodegradation is also determined by how many useful radicals can appear on the surface of nanoparticles per unit time and how much the surface of photocatalyst may interact with dye molecules, which in turn facilitates the degradation process[15].

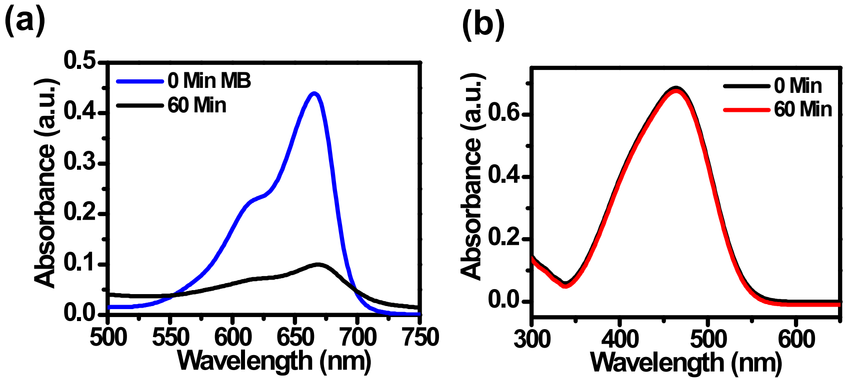

Figure S11. Remediation of dye from water by using *c*-BC@N-LCD. UV-vis absorbance spectra of a) MB, b) MO under solar irradiation.

16. Real-time outdoor demonstration for fresh water collection

To further demonstrate the practicality of *c*-BC@N-LCD hydrogel under real-time atmosphere, an outdoor experiment was conducted in a prototype evaporation device under natural sunlight in a sunny day from 10:00 to 17:00 on 14th October 2023. The outdoor solar evaporation device composed of an evaporation chamber with *c*-BC@N-LCD solar evaporator (one piece with diameter of 5.1 cm) was kept inside (Figure S12a). This device was laid on the roof of an experimental building exposed to sunlight. Within 10 min only it starts forming the vapours (Figure S12b). During the evaporation the vapours are formed and condensed as water droplets (Figure S12c) and collected at the bottom of the vessel Figure S12d. The variation of outdoor solar intensity, temperature and humidity for each hour are plotted in Figure S12e. The evaporation device shows the highest water production rate of 2.5 kg $m^{-2}h^{-1}$ at peak hour. An improved evaporation rate was observed here might be due to the less humidity and effect of wind which otherwise not present under laboratory experimental condition.

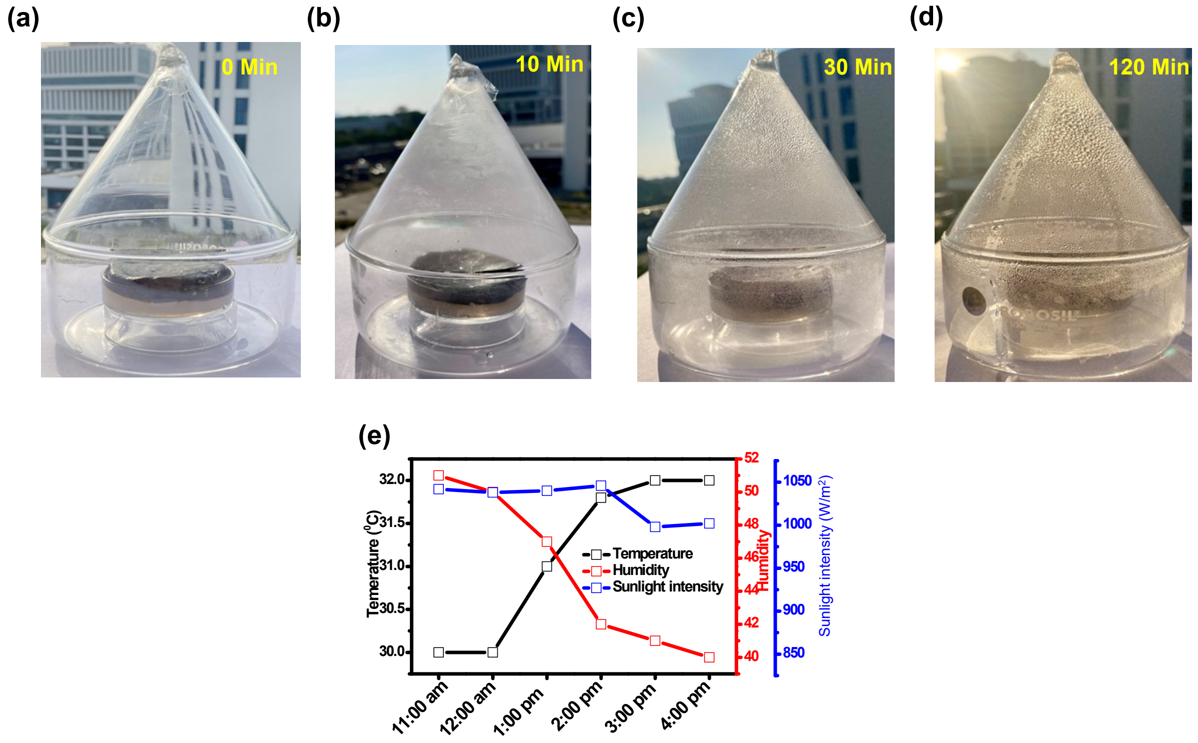

Figure S12. Demonstration of fresh water production with the aid of *c*-BC@N-LCD performed outdoor. Digital photographs taken (a) initially (t=0 min) and (b) after steam produced (t= 10 min). Formation of water droplets conical roof ensure formation and condensation of fresh water produced. (c) Formation, condensation (t=30 mins) and (d) collection of water droplets (t=120 mins). (e) Temperature, humidity, and intensity plots drawn from the values recorded in real time.

References

1 P. Zhao and L. Zhu, *Chem. Commun.*, 2018, **54**, 5401–5406.
2 G. Fei, Y. Wang, H. Wang, Y. Ma, Q. Guo, W. Huang, D. Yang, Y. Shao and Y. Ni, *ACS Sustainable Chem. Eng.*, 2019, **7**, 8215–8225.
3 B. Sun, J. Lin, M. Liu, W. Li, L. Yang, L. Zhang, C. Chen and D. Sun, *ACS Sustainable Chem. Eng.*, 2022, **10**, 1644–1652.
4 M. Xie, P. Zhang, Y. Cao, Y. Yan, Z. Wang and C. Jin, *npj Clean Water*, 2023, **6**, 1–9.
5 X. Hu, W. Xu, L. Zhou, Y. Tan, Y. Wang, S. Zhu and J. Zhu, *Advanced Materials*, 2017, **29**, 1604031.
6 Q. Zhang, L. Li, B. Jiang, H. Zhang, N. He, S. Yang, D. Tang and Y. Song, *ACS Appl. Mater. Interfaces*, 2020, **12**, 28179–28187.
7 T. Li, H. Liu, X. Zhao, G. Chen, J. Dai, G. Pastel, C. Jia, C. Chen, E. Hitz, D. Siddhartha, R. Yang and L. Hu, *Advanced Functional Materials*, 2018, **28**, 1707134.
8 H. Liu, C. Chen, H. Wen, R. Guo, N. A. Williams, B. Wang, F. Chen and L. Hu, *Journal of Materials Chemistry A*, 2018, **6**, 18839–18846.
9 X. Wang, Q. Gan, R. Chen, H. Peng, T. Zhang and M. Ye, *ACS Sustainable Chem. Eng.*, 2020, **8**, 7753–7761.
10 Y. Sun, X. Zong, D. Qu, G. Chen, L. An, X. Wang and Z. Sun, *Journal of Materials Chemistry A*, 2021, **9**, 7122–7128.

11 R. Chen, X. Wang, Q. Gan, T. Zhang, K. Zhu and M. Ye, *J. Mater. Chem. A*, 2019, **7**, 11177–11185.

12 S. Singh, N. Shauloff and R. Jelinek, *ACS Sustainable Chem. Eng.*, 2019, **7**, 13186–13194.

13 Z. Zheng, H. Li, X. Zhang, H. Jiang, X. Geng, S. Li, H. Tu, X. Cheng, P. Yang and Y. Wan, *Nano Energy*, 2020, **68**, 104298.

14 A. Peter, A. Mihaly-Cozmuta, C. Nicula, L. Mihaly-Cozmuta, A. Jastrzębska, A. Olszyna and L. Baia, *Water Air Soil Pollut*, 2016, **228**, 41.

15 C. Guillard, H. Lachheb, A. Houas, M. Ksibi, E. Elaloui and J.-M. Herrmann, *Journal of Photochemistry and Photobiology A: Chemistry*, 2003, **158**, 27–36.